

**Rare Isotope Accelerator
(RIA)
at
Michigan State University**

August 2003

1. Introduction.....	1
2. Driver Linac.....	1
2.1. Driver Linac Front End.....	3
2.1.1. ECR System.....	3
2.1.2. Low Energy Beam Transport (LEBT).....	3
2.1.3. Radio Frequency Quadrupole (RFQ).....	5
2.1.4. Medium Energy Beam Transport (MEBT).....	5
2.2. Driver Linac Superconducting Segments.....	6
2.2.1. Alternative Designs Considered.....	8
2.3. Linac Stripping Chicanes.....	10
2.4. Driver Linac Beam Dynamics.....	11
2.4.1. Transverse Beam Dynamics.....	12
2.4.2. Longitudinal Beam Dynamics.....	12
2.4.3. Transverse Misalignment and RF Errors.....	13
3. Beam Switch Yard (BSY).....	14
4. Isotope Separation On Line (ISOL) Station and Low-Energy Experimental Area.....	15
4.1. ISOL Target Stations and Low Energy ISOL Beam Transport.....	15
4.1.1. ISOL Station Layout and Front-end Systems.....	15
4.1.2. Mass Separation and Beam Transport.....	17
4.2. Post Accelerator.....	18
4.3. Experimental Areas.....	19
5. In-flight Separation, Gas Stopping, and High-Energy Experiments.....	20
5.1. Production Targets.....	21
5.2. Fragment Separators.....	21
5.3. Gas Stopping Station.....	22
5.4. High Energy Experimental Area.....	23
6. Summary.....	23
7. References.....	24

1. Introduction

The proposed Rare Isotope Accelerator (RIA) facility has had significant scrutiny by a large number of participants. In 1999 the Nuclear Science Advisory Committee (NSAC) ISOL (Isotope Separation On Line) Task Force was charged with providing a technical analysis of the various options for subsystems for an advanced ISOL facility. During these evaluations, Michigan State University (MSU) faculty proposed the paradigm utilizing a driver capable of accelerating all stable isotopes and using these beams to produce Radioactive Ion Beams (RIBs) by any of the known techniques including, ISOL and particle fragmentation. The ISOL beams would be used at low (keV) energies or accelerated to higher energies ($\sim 5\text{-}10$ MeV/nucleon). The particle fragmentation beams would be used at velocity (energies >50 MeV/nucleon) or stopped in a He gas cell and used at low (keV) or reaccelerated to higher energies ($\sim 5\text{-}10$ MeV/nucleon). This paradigm provides RIB production using the most efficacious approach for each experiment. The facility layout is given in Figure 1.

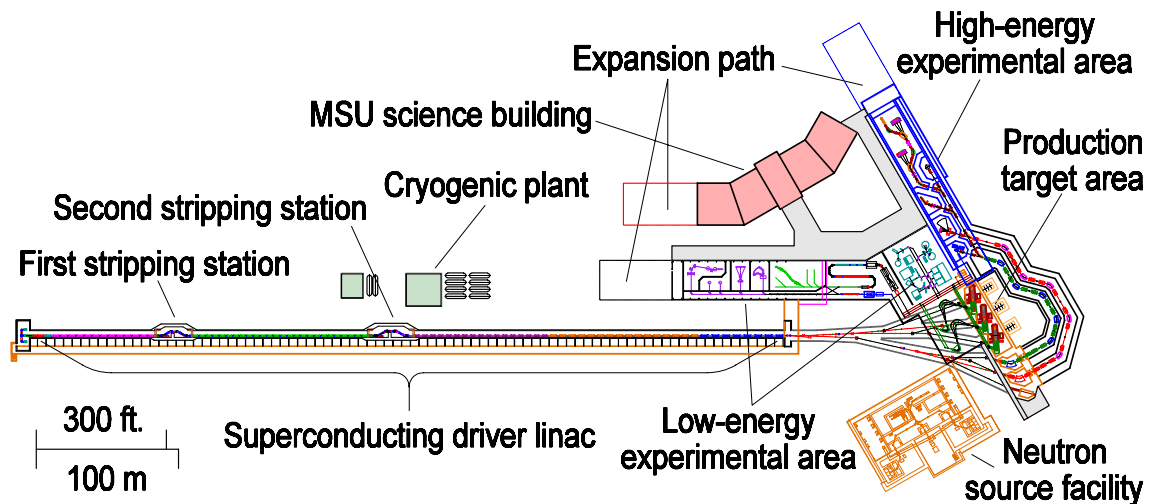


Figure 1. Overall layout of the RIA facility. The driver linac can have either a straight geometry (shown) or be folded based on optimization considerations.

The design of the individual components has certainly not been finalized. Alternatives for the superconducting accelerating structures, the primary beam distribution, the production targets and the experimental areas are being explored.

2. Driver Linac

A RIA driver workshop in 2000 made the decision to take advantage of the $\beta = 0.61$ and 0.81 superconducting accelerating structures being developed for the Spallation Neutron Source (SNS) project sited at ORNL.

The design proposed by ANL which was used for the Harrison NSAC sub-committee costing exercise was based on a 14th sub-harmonic (57.5 MHz) of the highest linac frequency (805 MHz). Such low frequency structures are susceptible to microphonics, and require significant rf power or, as proposed, a VCX tuner system. Reliability of the VCX tuner system has been an issue [1], and existing designs require liquid nitrogen cooling, posing an unnecessary oxygen deficiency hazard in the linac tunnel. In addition, the number of different cavity types proposed (9) was large.

Recently, at the second RIA driver workshop (2002) the MSU group presented alternatives for the driver linac design to the community. The design has been predominantly motivated by the minimization of technical risk and maximization of simplicity leading to higher probability of achieving performance and increased operational efficiencies.

MSU proposes a 10th sub-harmonic (80.5 MHz) accelerating lattice. The higher frequency has been shown to have significantly reduced microphonics allowing a simple solution utilizing a mechanical damper and modest rf [2] while avoiding the VCX tuner reliability concerns. The design requires only six (6) cavity types, and therefore, simplifies system R&D, design, fabrication, implementation, and operation.

The design is primarily determined by the requirement of a 400 MeV/nucleon uranium beam. For uranium, two charge states (28+ and 29+) will be extracted from the ECR and accelerated through the first linac segment to ≈ 12 MeV/nucleon. After stripping, the charge state distribution will be truncated to five charge states (73 ± 2) and further accelerated through a second linac segment to ≈ 90 MeV/nucleon where a final stripping will be performed. The charge state distribution will be truncated to three charge states (88 ± 1) and accelerated through a third linac segment to a final energy of 400 MeV/nucleon. The stripping locations were chosen to coincide with cavity frequency changes to provide improved longitudinal matching. The beam energy at the end of each linac segment for sample beams from protons through uranium is given in Table 1

Ion	A	Z	Segment I Energy (MeV/u)	Segment II Energy (MeV/u)	Segment III Energy (MeV/u)
H	1	1	11.8	239	1019
³ He	3	2	11.8	172	777
D	2	1	11.8	136	622
O	18	8	11.8	123	560
Ar	40	18	11.8	124	566
Kr	86	36	11.8	109	510
Xe	136	54	11.8	101	470
U	238	92	11.8	89	400

Table 1. Beam energies by linac segments.

2.1. Driver Linac Front End

The driver linac front end includes Electron Cyclotron Resonance (ECR) ion sources, a Low Energy Beam Transport (LEBT), and a buncher system feeding a Radio Frequency Quadrupole (RFQ). A Medium Energy Beam Transport (MEBT) system following the RFQ is used to match the RFQ beam into the superconducting accelerating lattice of the driver linac. Figure 2 shows the layout of the driver linac front end.

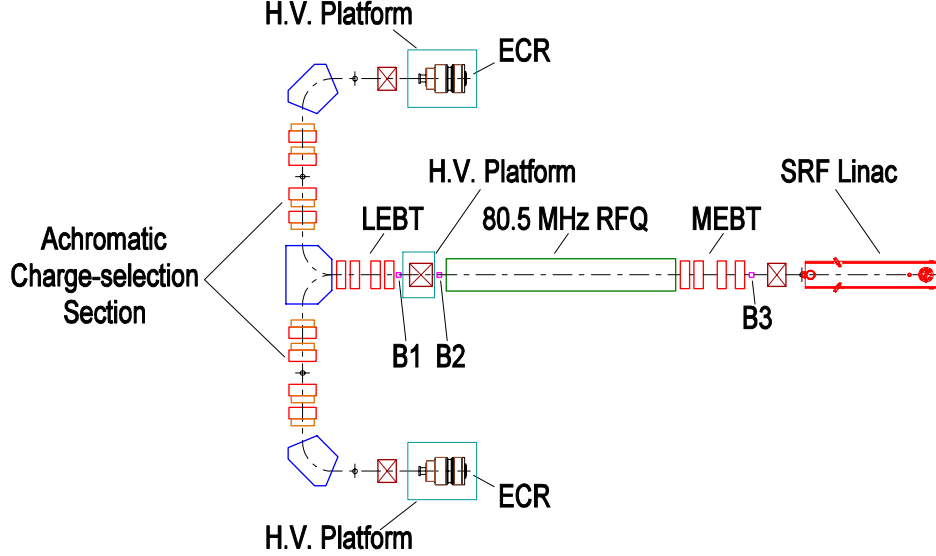


Figure 2. The layout of the driver linac front end.

2.1.1. ECR System

The ECR System will include several (≥ 2) ECR sources with high voltage platforms of approximately 100 kV and a downstream beam transport providing charge state selection and emittance measurement capabilities. Several ECRs will be needed to ensure reliability through redundancy, provide the opportunity to have specialized ECRs for specific beam (e.g., metallic or gas) optimization, and to provide the opportunity for off-line beam development.

2.1.2. Low Energy Beam Transport (LEBT)

Following the ECR achromatic charge-mass selection section, the LEBT system will be used to transport and match the beam transversely to the RFQ. The LEBT will also provide longitudinal bunching of the dc beam from the ECR into a bunched beam for the RFQ for both single and two-charge state beams. To meet the beam power requirements, two-charge-state-beam injection is necessary for ions heavier than xenon ($A > 136$). The typical beam parameters are listed in Table 2. The voltage of the ECR platform (V_{ECR}) is adjusted to achieve the same beam velocity for different ions (same average velocity as the case of two-charge-state beams).

The LEBT uses four electrostatic quadrupoles and a solenoid magnet to provide transverse focusing and phase space matching. A multi-harmonic buncher (B1) will produce a near linear energy modulation for beam bunching. The quadrupoles convert the

asymmetric beam from the upstream analysis section to an axially symmetric beam at B1 with the solenoid maintaining the symmetry up to the RFQ. For two-charge-state-beam injection, a velocity equalizer (B2) [3] is employed before the RFQ to adjust the velocities of the two charge states. A bipolar high-voltage platform between B1 and B2 is also utilized to provide proper longitudinal separation for two-charge-state operation of various ions heavier than xenon ($A \geq 136$). To simplify the system design and future operation, both B1 and B2 are located off the high-voltage platform.

Ion	A	Q	V_{ECR} (kV)	I_{ECR} (μA)	Final Beam Power (kW)	
					One-charge State beam	Two-charge State beam
H	1	1	12.0	540	400	-
Xe	136	17	95.8	12.0	400	-
Au	197	23&24	100.4	5.5	241	483
U	238	28&29	100.0	1.5	77	154

Table 2. Sample beam parameters.

For single-charge-state beams, the buncher (B1) will operate at a fundamental frequency of 80.5 MHz, and neither the velocity equalizer B2 nor the high-voltage platform between B1 and B2 are required. For two-charge-state beams, the buncher (B1) will operate at the fundamental frequency of 40.25 MHz (half of the RFQ frequency). Both the velocity equalizer (B2) and the bipolar high-voltage platform are required. Table 3 shows the LEBT hardware requirements for two-charge-state operations. Simulation results for the two-charge-state uranium beam are given in Figure 3.

Ion	A	Q	V_p (kV)	Buncher Voltage (kV)	
				B1 (1 st harmonic)	B2
Xe	136	19 & 20	-52.38	1.242	1.754
Au	197	23 & 24	0	2.134	2.135
U	238	28 & 29	+38.95	2.728	2.141

Table 3. LEBT two-charge-state operation parameters.

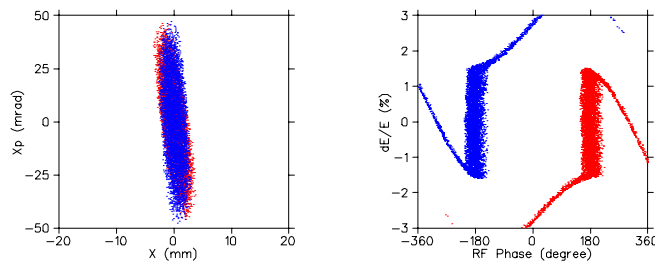


Figure 3. Horizontal (left) and longitudinal (right) phase space distributions at the entrance of the RFQ for two-charge-state beam of ^{238}U . [blue (29+), red (28+)]

2.1.3. Radio Frequency Quadrupole (RFQ)

The RFQ will have a frequency of 80.5 MHz appropriate for the 10th sub-harmonic superconducting accelerating lattice, an input energy of 12 keV/u and an output energy of 292 keV/u. The initial energy corresponds to an ECR platform voltage of approximately 100 kV. The final energy corresponds to a transit time factor of 0.5 for the first superconducting cavity in the driver linac. The RFQ parameters are given in Table 4. The peak field value is 1.71 Kilpatrick, below the LEDA RFQ value of 1.8 Kilpatrick.

For an initial beam with rms normalized transverse emittance $\epsilon_{x,y} = 0.103 \pi \cdot \text{mm} \cdot \text{mrad}$ and longitudinal emittance $\epsilon_z = 0.342 \pi \cdot \text{keV/u} \cdot \text{ns}$, we have obtained output values (first number for 28+, second number for 29+) of $\epsilon_{x,y} (\pi \cdot \text{mm} \cdot \text{mrad}) = (0.1, 0.1)$ and $\epsilon_z (\pi \cdot \text{keV/u} \cdot \text{ns}) = (0.084, 0.09)$ with a total transmission of (99.27%, 99.28%) and an effective transmission (accelerated) of (94.07%, 94.20%). (A non-accelerated continuous beam (~5% of the total), will cross the RFQ and will be lost in the matching section between the RFQ and the superconducting part.) These calculations show that the transverse beam dynamics is very similar for the two charge states in the RFQ (assuming identical input Courant-Snyder parameters). For the longitudinal plane, the difference between the two charge states is more important but remains reasonable. The energy shift between the two charge states is equal to 16% of the maximum energy spread [4].

Parameter	Value
Length	3.07 m
Mean radius R_0	6.5 mm
Transverse electrode curvature ρ	$0.8 \times R_0$
Minimum aperture a	$6.19 \rightarrow 4.44 \text{ mm}$
Modulation factor m	$1.1 \rightarrow 1.92$
Synchronous phase Φ_s	$-25^\circ \rightarrow -20^\circ$
Voltage	90 kV
Number of cells	123

Table 4. 80.5 MHz RFQ parameters.

2.1.4. Medium Energy Beam Transport (MEBT)

The MEBT will be used to transport and match the beam to the driver linac's superconducting accelerating lattice. The asymmetric beam from the RFQ is transformed into a round beam by using four magnetic quadrupoles. Together with the quadrupoles, a superconducting solenoid magnet before the superconducting accelerator provides transverse focusing and phase space matching. An 80.5 MHz, $\beta = 0.0251 \lambda/4$ resonator (B3) near the middle of the MEBT will be used to match the longitudinal phase space into the superconducting linac.

The beam dynamic studies of this section were done primarily for two-charge-state (28+, 29+) uranium beams. The electromagnetic field-map of the quarter wave resonator (B3) was obtained from SUPERFISH. Figure 4 shows PARMELA simulation results for the transverse and longitudinal phase space distribution for a 28+ uranium beam.

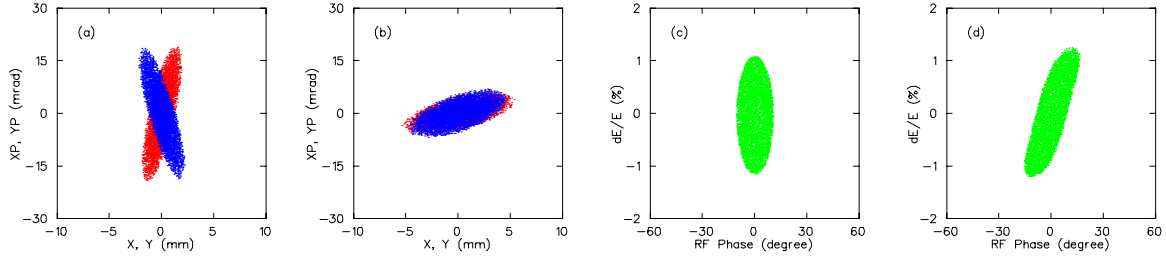


Figure 4. Transverse and longitudinal phase space distribution of 28+ uranium beam at the exit of RFQ (a,c) and at the entrance of SRF linac (b,d). Horizontal (red), Vertical (blue), and Longitudinal (green).

2.2. Driver Linac Superconducting Segments

The driver linac will have three segments separated by two stripping systems. The first section – designated Linac I – will accelerate particles to beam energies of about 12 MeV/nucleon. Since this section of the linac is the most challenging, it is proposed that it be operated in a constant velocity mode for all beams. This simplifies operations since only cavity voltage needs adjustment. The penalty is a minor energy reduction of the final energy of the lighter elements. For example, the final proton energy will be reduced by about 7 MeV/nucleon to approximately 1019 MeV/nucleon under this assumption. Linac I will be followed by a stripping chicane consisting of a stripping target, a magnetic chicane to provide for the removal of unwanted charge states, and rebuncher sections. The second linac segment – designated Linac II – will accelerate uranium to ≈ 90 MeV/nucleon at which point a second stripping system will be used to increase the average charge state and to remove unwanted charge states. The final linac segment – designated Linac III – will accelerate uranium to 400 MeV/nucleon.

The required cavity types are described in Table 5 and shown in Figure 5. The transit time curves and energy gain are shown in Figure 6 for uranium and Figure 7 for protons. A typical cryostat unit for the $\lambda/2$ and $\lambda/4$ structures (segments I and II) incorporating superconducting solenoidal focusing and isolated vacuum is shown in Figure 8. The cryostat for elliptical structures (segment III) will have cryostat units as shown in Figure 9. Room temperature quadrupole doublets are used between cryomodules in segment III.

Cavity Type	β_{opt}	f (MHz)	Peak E field (MV/m)	T (K)	Linac Segment	# Of Cavities	# Of Cryostats
$\lambda/4$	0.041	80.5	16.5	4.2	I	18	2
$\lambda/4$	0.085	80.5	20	4.2	I	104	13
$\lambda/2$	0.285	322	25	2	II	208	26
Elliptical	0.49	805	32.5	2	III	68	17
Elliptical	0.63	805	32.5	2	III	64	16
Elliptical	0.83	805	32.5	2	III	32	8

Table 5. Driver linac cavity lattice.

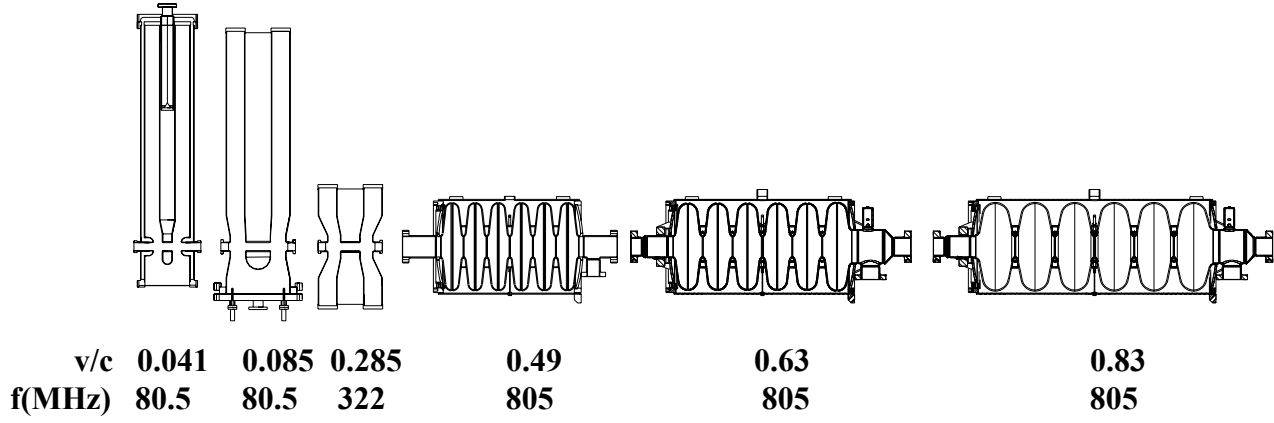


Figure 5. Driver linac cavity types.

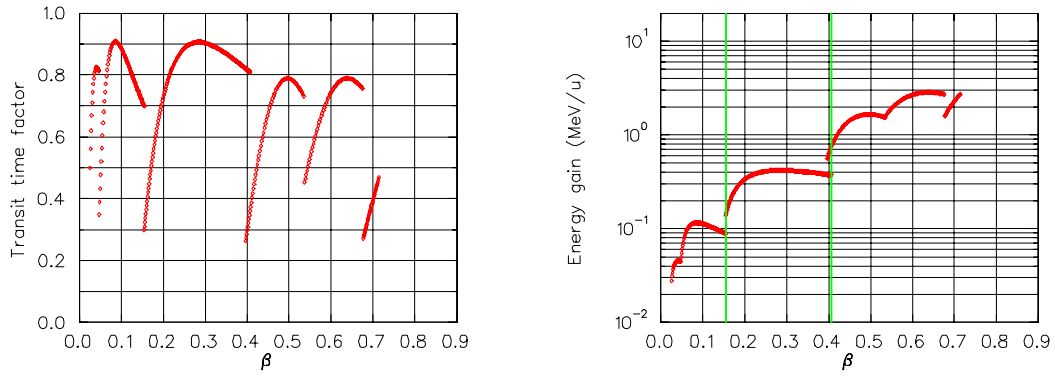


Figure 6. Transit time factors and energy gain for uranium.

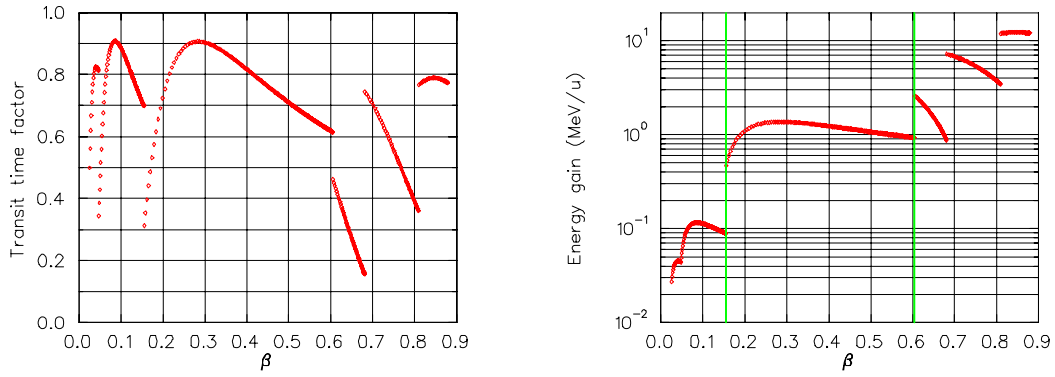


Figure 7. Transit time factor and energy gain for protons.

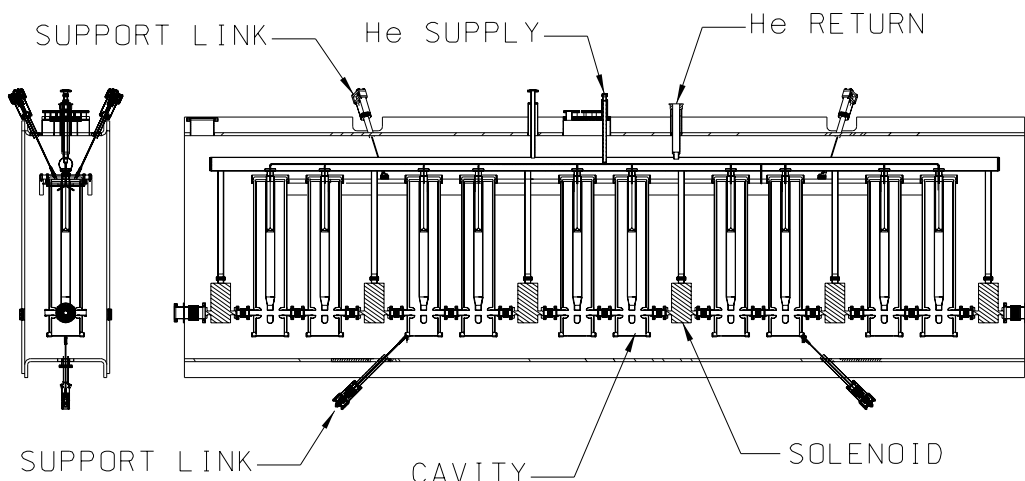


Figure 8. Layout of linac segment I cryostat for $\beta=0.041$ cavities. Cryostats for $\beta=0.085$ and 0.285 in linac segments I and II are similar.

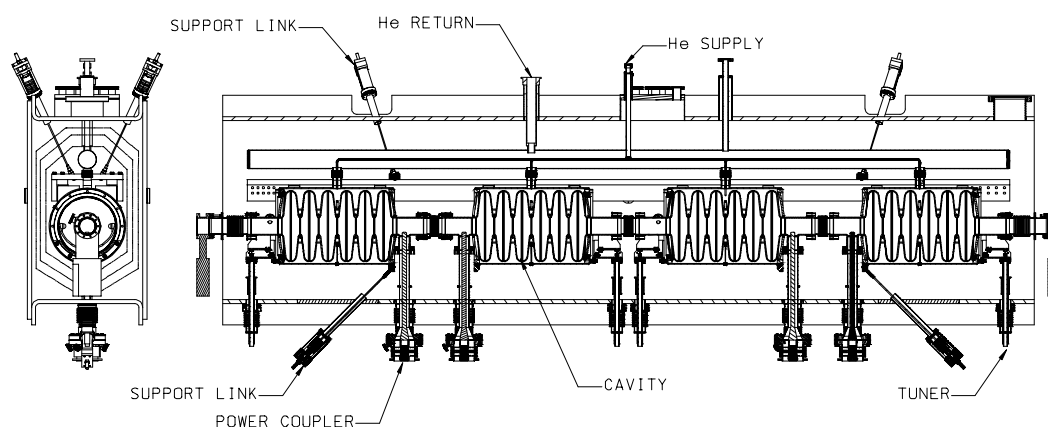


Figure 9. Layout of linac segment III cryostats.

2.2.1. Alternative Designs Considered

2.2.1.1. Accelerating Structures

A series of alternative accelerating lattices was considered. Among them was the ANL proposed 14th sub-harmonic (57.5 MHz) system. This comparison is documented in presentations at the RIA Driver Workshop II (May 2002). The salient issues are:

- The 14th sub-harmonic design required nine (9) cavity designs with five different geometries (fork, $\lambda/4$, $\lambda/2$, double spoke, and elliptical). The 10th sub-harmonic design of Table 5 requires only six (6) cavity types with three different geometries, all of which will be prototyped or otherwise extant by the end of 2003.
- The 14th sub-harmonic design requires a VCX tuner for the lowest frequency cavities with its reliability issues and the oxygen deficiency hazard of liquid nitrogen in the tunnel. The 10th sub-harmonic with a mechanical damper does not require VCX tuners as demonstrated by Legnaro INFN operational experience. VCX turners above

100 MHz do not yet exist and would need to be developed should the 14th harmonic lattice double-spoke require a VCX tuner.

- The ratio of the longitudinal acceptance to beam emittance is five (5) for the 10th harmonic solution and only 13% less than that of the 57.5 MHz solution. The transverse acceptance is the similar for both cases.

A proposal to utilize triple spoke structures in lieu of the SNS and SNS-like elliptical structures was also evaluated [5]. The triple spoke structures do not exist so their performance can only be estimated. The elliptical structures have significant and well-documented experimental data. For the large diameter (7.7 cm) elliptical structures, a simple quadrupole doublet in the warm region provides good performance. The smaller diameter triple-spokes (3-5 cm) require more complex and expensive 9 T superconducting solenoids to achieve appropriate transverse beam control.

2.2.1.2. Cavity Operating Temperatures

The effect of the cavity operating temperatures and a comparison between elliptical and triple-spoke structures for the last linac segment were explored. We estimated the size, capital cost, and wall plug power usage of the cryo-plant required to operate the linac. An intrinsic quality factor (Q_0) of $2.5 \cdot 10^8$ was assumed for cavities operating at 4.2 K; a Q_0 of $5 \cdot 10^9$ was assumed for cavities operating at 2 K. A static heat leak of 25 W per cryostat was assumed. The total refrigeration load includes an additional 50% for the distribution system and contingency. The wall plug power is obtained from the refrigeration load via the product of the Carnot efficiency and the technical efficiency. The technical efficiency values used are based on experience at CEBAF [6]. The overall efficiency decreases by a factor of 3.5 as the temperature decreases from 4.2 K to 2 K. The capital cost of the cryo-plant is assumed to scale with the cryogenic load to the 0.7th power consistent with recent experience for large cryo-plants [7]. Correspondingly the cost for a 2 K cryo-plant is a factor of 2.3 higher than that of a 4.2 K cryo-plant. Inflation was also factored in to convert values to 2003 dollars.

Linac Lattice	Cryogenic Plant			
	4.2 K Capacity (kW)	2 K Capacity (kW)	Wall Plug (MW)	Cost (M\$)
Lattice of Figure 5, $\lambda/4$ & $\lambda/2$ @ 4.2K, ellipticals @ 2K	16.3	13.4	14.9	41
Lattice of Figure 5, $\lambda/4$ @ 4.2K, $\lambda/2$ & ellipticals @ 2K	2.7	15.2	13.2	34
Lattice of Figure 5 for ($\lambda/4$ & $\lambda/2$) & triple-spokes @ 4.2K (no ellipticals)	66.8	0	15.7	37

Table 6. Cryogenic plant requirements for driver linac variants.

The results of these analyses are given in Table 6, concluding that cryogenically the most effective option is the proposed linac using the cavities of

Figure 5 with the $\lambda/4$ at 4.2K and all other cavities ($\lambda/2$ & ellipticals) at 2 K.

2.3. Linac Stripping Chicanes

The charge-stripping sections will increase the average charge state, provide elimination of unwanted charge states, and provide 6D matching into the next linac segment.

After the 1st charge-stripping station, ^{238}U will have an energy of 11.60 MeV/u ($B\rho=1.60\text{ T}\cdot\text{m}$). Five charge states (71+ to 75+) will be retained and transported to the second driver linac segment. The beam energy will be 83.8 MeV/u ($B\rho=3.64\text{ T}\cdot\text{m}$) after the 2nd charge-stripping station. Only three charge states (87+ to 89+) will be retained for further acceleration.

The optical system has 4 identical cells with 4-fold symmetry. An rf buncher in the center provides the longitudinal beam bunch control. Two quadrupole triplets in each cell are used to achieve the 1st order optical conditions for a 2nd order achromat. The system has excellent 2nd order optical properties due to its high symmetry. No 2nd order geometric aberrations exist and there are only four chromatic terms, which can be completely cancelled by 4 correction sextupoles per cell. Perturbations from 3rd and higher order aberrations are small.

Figure 10 shows the layout of the 1st charge-stripping chicane. The total length of the chicane is 24.1 m. A single $\lambda/4$ cavity with frequency of 80.5 MHz and β_{opt} of 0.085 will be used as the rf buncher. The transverse phase space distribution at the beginning and end of the 1st charge-stripping chicane for ^{238}U beam are shown in Figure 11.

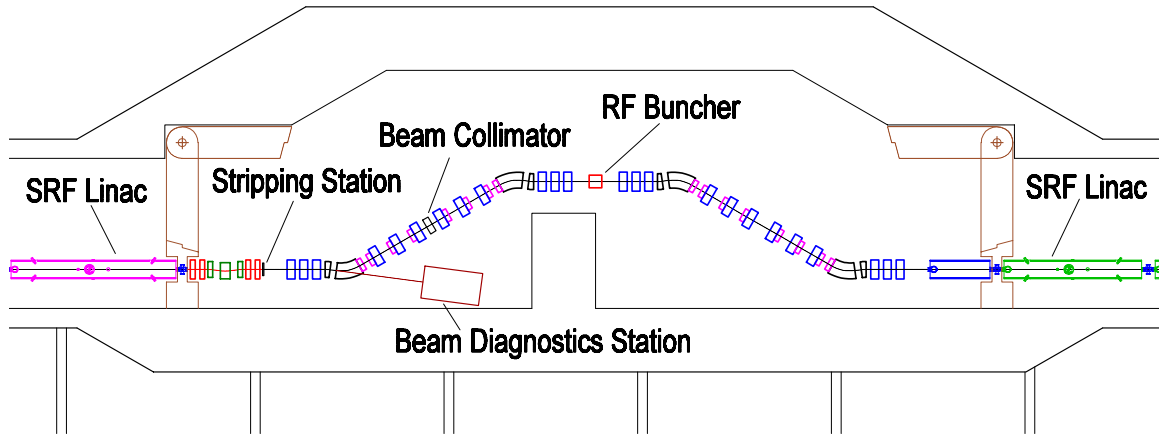


Figure 10. The layout of the 1st charge-stripping chicane for RIA driver linac.

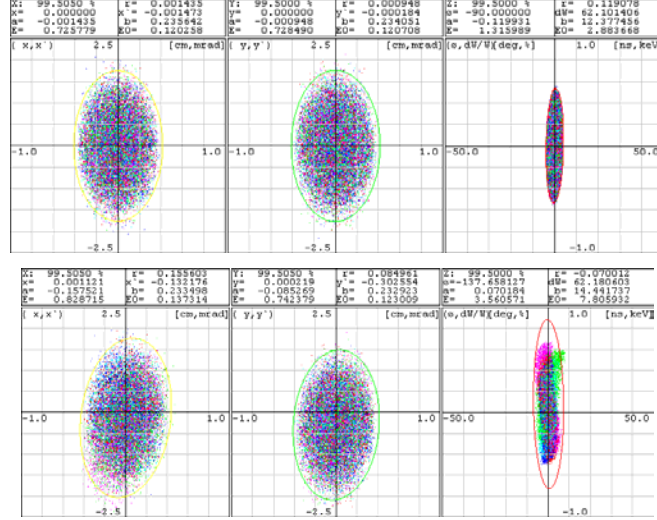


Figure 11. Horizontal (left), vertical (middle) and longitudinal phase space distributions for ^{238}U beam at beginning (top) and end (bottom) of the 1st charge-stripping chicane.

The layout of the 2nd charge-stripping chicane is similar to the first. Four $\lambda/2$ cavities with a frequency of 322 MHz and β_{opt} of 0.285 will be used as the rf buncher.

The transverse emittance of both planes increases nearly linearly with the magnet position errors for both stripping chicanes. However, the rotation error (σ_{zt}) strongly impacts the vertical emittance while the effect is small in the horizontal plane. For the alignment criteria given in Table 7, the average transverse emittance growths were <30% in each chicane.

Chicane	Position $\sigma_{x,y}$	Rotation σ_{zt}
1 st	0.5 mm	0.5 mrad
2 nd	1.0 mm	0.5 mrad

Table 7. Misalignment tolerances for the two charge-stripping chicanes.

2.4. Driver Linac Beam Dynamics

The rf defocusing strength from all 6 types of SRF cavities used in the driver linac was found to be an order of magnitude smaller than that of the lattice focusing elements. As a consequence, the transverse beam dynamics are predominantly determined by the focusing elements and lattice layout. The coupling between the beam longitudinal and transverse motion was found to be inconsequential in the driver linac beam dynamics. In addition, extensive studies of the parametric 2nd order coupling resonance and associated transverse emittance growth in the high-energy part of the linac were carried out, and showed no observable effect in our design option of the driver linac [8, 9].

The results of the beam dynamics studies show that the 10th subharmonic (80.5 MHz) driver linac option has adequate transverse and longitudinal acceptance for multi-charge-state beam acceleration with required final beam energy and power. The acceptances are

primarily determined by the first few cryostats where the beam energy is low and transverse and longitudinal focusing is most important. Reasonable misalignment and rf error specifications provide no beam loss and acceptable emittance growth. [10, 11]

2.4.1. Transverse Beam Dynamics

Transverse beam dynamics studies included establishing an adequate focusing lattice for each linac segment with reasonable hardware requirements, studying the impact of misalignment of lattice elements, and exploring correction schemes. All three segments of the MSU driver linac design were found to have adequate transverse acceptance within specified misalignment and rf errors.

2.4.1.1. Segment I of driver linac

The transverse focusing is accomplished with 76 superconducting solenoid magnets. The SRF cavities are low- β $\lambda/4$ cavities with a frequency of 80.5 MHz and a diameter of 30 mm. To control the initial beam size and avoid beam loss where the beam energy is low and emittance is large, the transverse phase advance per cell in the first two cryomodules is about 90° . Because of adiabatic damping, the phase advance is allowed to gradually decrease to about 25° at the end of segment I to limit the required superconducting solenoid magnet field to less than 9 Tesla.

2.4.1.2. Segment II of driver linac

The transverse focusing is accomplished with 52 superconducting solenoid magnets. The SRF cavities are low- β $\lambda/2$ cavities with a frequency of 322 MHz and a diameter of 30 mm. The maximum required solenoid magnet field is about 8 Tesla to maintain the transverse phase advance per cell of $\sim 85^\circ$.

2.4.1.3. Segment III of RIA driver linac

The transverse focusing is accomplished with room-temperature quadrupoles positioned between cryomodules. The SRF cavities are high- β 6-cell elliptical cavities with a frequency of 805 MHz and a diameter of 77 mm. The quadrupoles have an diameter of 5 cm, length of 0.25 m, and a maximum pole tip magnetic field of about 0.6 T.

2.4.2. Longitudinal Beam Dynamics

The cavities were independently phased with respect to each other to achieve equivalent $\phi_s \approx 30^\circ$ and minimal emittance growth of multiple charge state beams.

Figure 12 shows the evolution of the longitudinal emittances for individual charge states as well as for the effective overall emittance along the linac. The primary degradation of the overall longitudinal acceptance is imposed by the low energy part of the linac. No observable degradation of the overall longitudinal acceptance was found for the 2nd and 3rd linac segments. Accelerating rf field errors of 0.5% in amplitude and 0.5° in phase were found to provide acceptable performance.

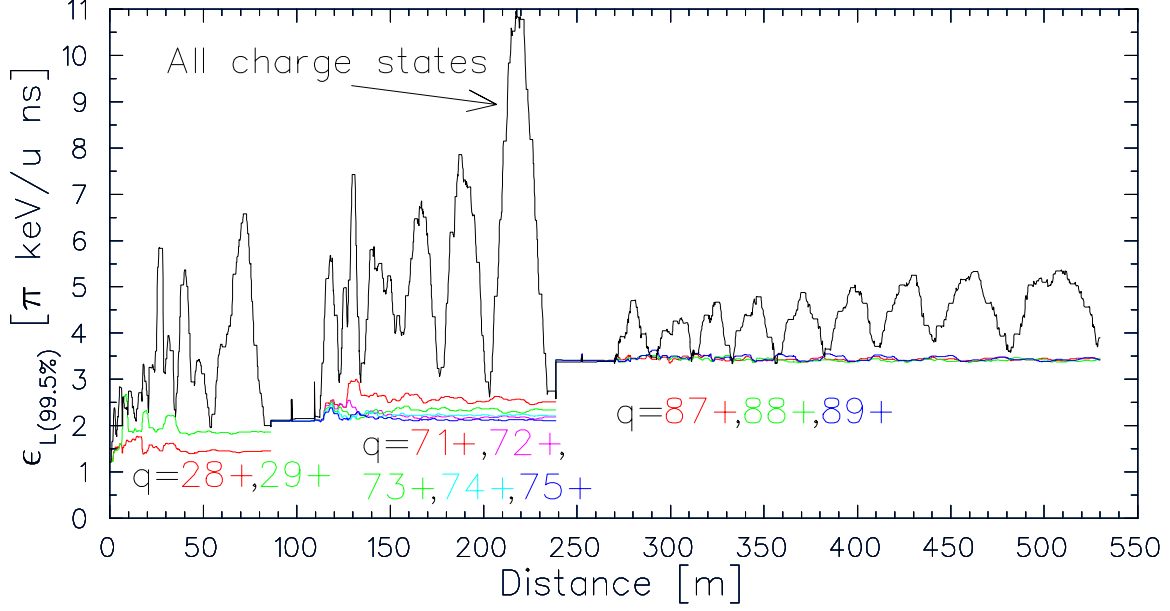


Figure 12. Longitudinal emittance evolution for separate charge states and for all charge states together along the linac.

2.4.3. Transverse Misalignment and RF Errors

The lattice sensitivity to misalignment of focusing elements and cavities was investigated. All accelerating structures and focusing elements were assumed to be misaligned with a Gaussian distribution ($\pm 2\sigma$). The strong magnetic fields required for the superconducting solenoids in segments I and II, and the quadrupoles in segment III were found to be more sensitive to misalignment errors than the SRF cavities in the lattice.

Given the misalignment tolerances listed Table 8, with a 90% confidence, the maximum orbit distortions will be limited within ± 5 mm, and the transverse beam emittance growth will be 10 to 20% in all three parts of the driver linac. No beam loss was observed in the simulations with 2×10^5 particles tracked due to misalignment errors.

RIA Driver Linac	SRF Cavity Misalignment		Focusing Element Misalignment	
	$\sigma_{x,y}$ (mm)	σ_{zr} (mrad)	$\sigma_{x,y}$ (mm)	σ_{zr} (mrad)
Part I	1.0	-	0.25	-
Part II	1.0	-	0.50	-
Part III	1.0	-	1.00	5.0

Table 8. Linac alignment tolerances.

When the random rf errors (0.5° in phase and 0.5% in amplitude) were combined with the misalignment errors, only the longitudinal rms emittance growth increased, indicating weak coupling between the transverse and longitudinal motion. No additional beam loss due to the combined misalignment and rf errors was observed.

3. Beam Switch Yard (BSY)

The general design requirements are delivery of multiple charge states of a single isotope to at least two simultaneous targets. A more complete analysis of the target region requirements has resulted in the determination that a larger horizontal spread is needed to accommodate the required target area infrastructure. This result and the desire to increase operational efficiency have led to a proposed BSY design for up to four targets receiving beam simultaneously. Figure 13 shows the driver beam switchyard layout. The beam from the driver linac first goes through an rf kicker-dipole-septum system where beam can be divided into two with 50% beam power each by the rf kicker; or switched into either one with 100% of beam power by a dipole. Downstream, another rf kicker-dipole-septum system will further split or switch beams into the final four beam lines. Additional dipoles and quadrupole magnets will be used to guide and focus beams onto the ISOL and fragmentation targets. Table 9 lists the beam delivery possibilities of the beam switchyard design.

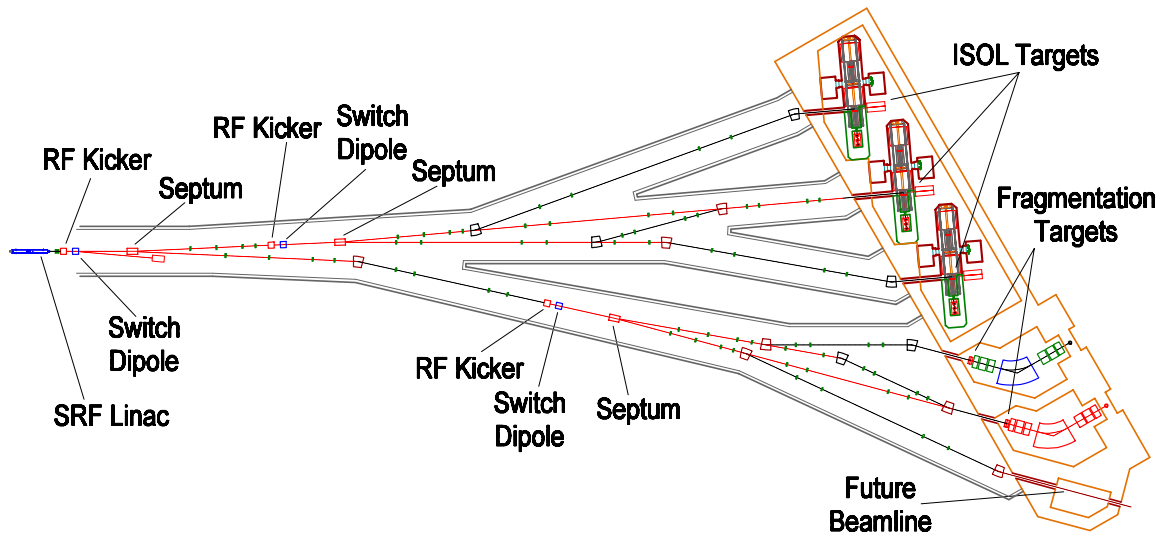


Figure 13. The layout of the RIA beam switchyard.

Beam Power Split	RIA Target Stations
100%	Any one
50%, 50%	Any two
50%, 25%, 25%	Any three
25%, 25%, 25%, 25%	Any four

Table 9. Beam delivery capabilities of the beam switchyard.

4. Isotope Separation On Line (ISOL) Station and Low-Energy Experimental Area

Beams from the ISOL stations are mass separated and either delivered to the experimental area for stopped beams or to the post-accelerator for low-energy beam experiments. MSU's concept optimizes the use of the available primary beams and focuses on reliability in operation and on flexibility.

4.1. ISOL Target Stations and Low Energy ISOL Beam Transport

ISOL target stations with the capability to receive primary beam power of 400 kW are considered. This will be an order of magnitude more power handling capability than realized at ISAC, the highest-power ISOL facility presently operational. It is generally accepted that with today's technology and know-how it will be possible to build target systems for beam powers up to 100 kW. Target systems accommodating 400 kW beam power are not possible with current technology, though R&D over the next decade may achieve this goal. Therefore, the proposed design implements the necessary shielding and infrastructure capabilities suitable for 400 kW beam operation.

Three ISOL target stations are necessary for efficient operations including beam development. A two-station scenario was proposed in the very early stage of RIA planning, however such a scenario does not provide important redundancy and will hinder any active beam development program and R&D toward the highest power targets. (ISAC, for example, is just upgrading from two to three stations).

The ISOL beam handling system includes pre-separators, high-resolution separators and beam line matrices for a beam transport to the experimental areas and the post-accelerator (Figure 14). The present layout maximizes the usability of the ISOL beams produced in any of the stations.

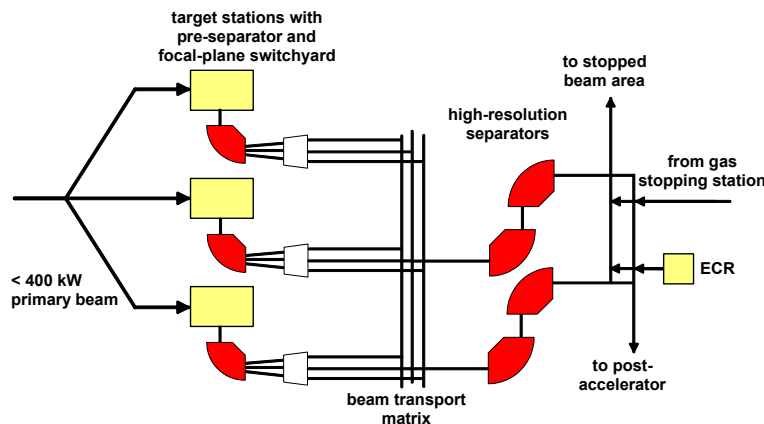


Figure 14. General concept for the ISOL facility of RIA.

4.1.1. ISOL Station Layout and Front-end Systems

Key design considerations were a maximum beam power of 400 kW, target changes with minimum downtime, good radioprotection, and a high flexibility with respect to implementing new target concepts.

One option for a layout of the target stations is to adopt a system similar to the one realized at ISAC based on vertical modules. Advantages of this system are its modularity, a small footprint, and that it has proven to be a practical solution at an ISOL facility using already a few ten kW beam power. Another option is a horizontal system in which the critical components are installed on a cart system. Such a concept comes closer to those of other high power target systems like the 1 MW spallation neutron source SNS at Oak Ridge, ISIS at RNL/Rutherford or the SIRIUS project once proposed for RNL. Compared to a vertical system, a horizontal system has a larger footprint, but this mitigates the uncertainty of what high-power target configurations will eventually be implemented.

Figure 15 illustrates the conceptual layout for a horizontal ISOL system. Target and ion source system and probably also part of the front-end are mounted on a cart that can be retracted into a service position. Two-sided remote handling access will allow target changes and small system maintenance to be performed directly in the target vault. Shielding plugs above the vault make it possible to bring down new targets and to remove old target units and take them to the target service bay for packing and transport to a storage site. The vertical opening can be stepwise increased to allow the removal of larger pieces for major maintenance or replacement. An attractive feature of this concept is that only those parts are removed from the vault for which there is a necessity. This is expected to reduce the time needed for target changes and to have positive aspects with respect to radioprotection.

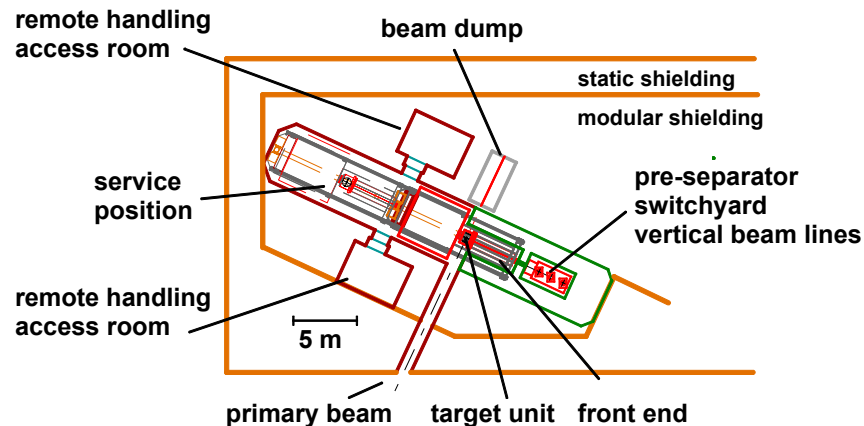


Figure 15. Layout of a horizontal ISOL system for RIA.

The three vaults for the ISOL target stations are arranged as compactly as possible while still allowing remote work in one target area even when beam is sent to a neighboring one (see Figure 16). The horizontal system is more complex than vertical plugs and a detailed analysis of both systems or a hybrid should still be made. In any case, the space allocated is sufficiently large to incorporate any solution.

Since advanced 400 kW systems may not be initially available, a staged approach to ISOL implementation is likely the best choice. Depending on the advances made in target R&D, scenarios can be imagined where two stations are equipped to handle lower-power

systems (≤ 100 kW) while the third station is used to develop a prototype for the final high-power system to which the other stations can be upgraded at a later stage.

For the ISOL front-end system, it will be important to make the design such that very different types of targets can be coupled including those that may require liquid metal cooling or which are themselves liquid metal targets or target/catcher systems for heavy ion primary beams.

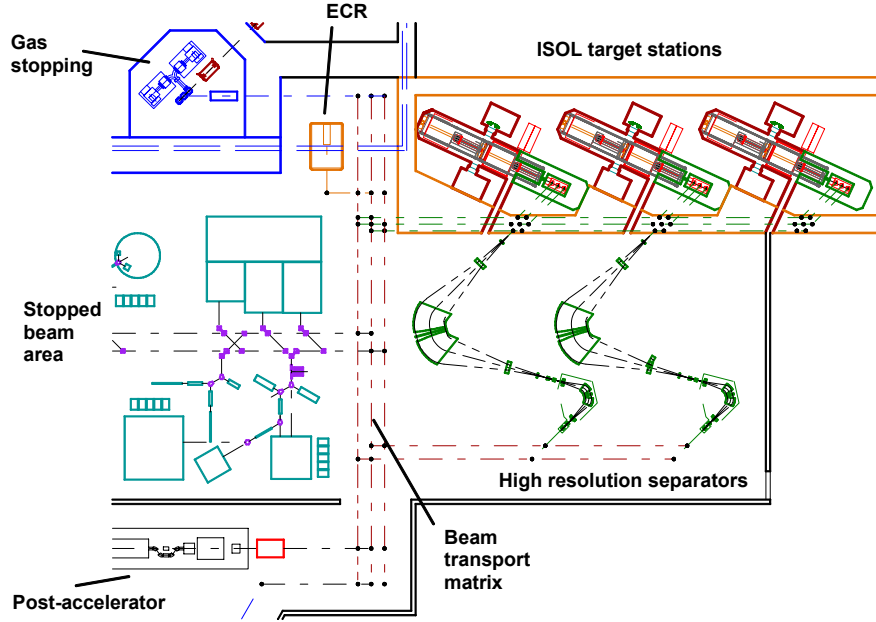


Figure 16. Layout of the ISOL area of RIA.

4.1.2. Mass Separation and Beam Transport

Downstream of the front-end systems the ion beams will be pre-separated in magnetic dipoles that are oriented vertically and well shielded from the target area. A focal plane switchyard allows a central mass and one lower and one higher mass beam to be selected and sent into three beam lines. Cryogenic panels in the beam lines retain radioactive gases coming from the ISOL targets. At ground level the vertical beam lines from all stations connect to a beam line matrix that allows each beam to be sent to one of the two high resolution mass separators or to collection points for isotope harvesting. For the high-resolution separators a design made ANL [12] has been used, but these separators have a very large footprint and are technically challenging and costly. Future R&D on beam cooling may show that more compact solutions could be used. Each of the high-resolution separators has one short connection to one ISOL station to have one combination that can be expected to have the best ion optical performance. The beams from the separators can either be sent to the experimental area for the stopped beams or to the post-accelerator for low-energy beam experiments. An ECR ion source will provide stable test beams. The beam distribution system after the high-resolution separators will

also connect to a line through which the rare isotopes from the gas stopping station are delivered.

4.2. Post Accelerator

The post accelerator for RIA will provide beams of 8 MeV/u for all masses up to $A=240$ and up to 20 MeV/u for light masses ($A < 60$). The beams to be post-accelerated are delivered either from the gas stopping station or from the ISOL stations as mostly singly charged ions with beam energy of 80 keV.

The design of the post-accelerator is based on significant developments at ANL, TRIUMF and MSU. Figure 17 shows a block diagram of the post accelerator and Table 10 gives some parameters. Frequencies chosen are based on using one of the MSU driver linac frequencies, 80.5 MHz, a sub-multiple of the main 805 MHz frequency used for most of the driver linac concept.

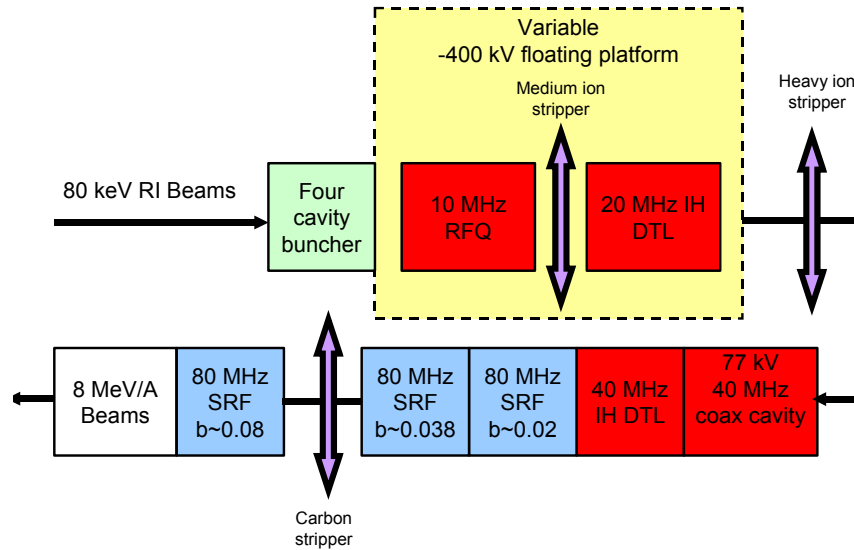


Figure 17. Schematic layout of the post accelerator.

Important characteristics of the post-accelerator are large acceptance, adequate beam intensity within an acceptable transverse input emittance, good energy resolution for the output beam and a good timing structure associated with a good longitudinal emittance. Initial acceleration stages are based on room temperature structures [13, 14, 15]. After passing a 4-stage bunching system, the 80 keV dc beam is transported to an RFQ and IH drift tube linac. Both are located on a floating platform to ensure good capture in the RFQ, which is based on a split coaxial geometry [16]. Following the RFQ is an interdigital IH drift tube linac similar to those developed at GSI [17], TRIUMF and at ANL. The output energy from the RFQ of about 8 keV/u was partly chosen because of a desire to strip only the medium mass ions to a 2+ state by a He gas stripper at this point. Heavy ions are stripped after the IH drift tube linac at 20 keV/u to a 4+ state after the beam has left the high voltage platform. This scenario ensures that the following IH drift tube section has good beam quality with input Q/A ratios better than 1/66. A coaxial

loaded cavity adjusts the ion velocities for the injection into the 40.25 MHz IH DTL that raises the energy of the beam to 100 keV/A. Remaining portions of the linac are all 80.5 MHz superconducting $\lambda/4$ structures developed at MSU [18]. Sixteen cavities of $\beta \sim 0.02$ geometry and 34 cavities of $\beta \sim 0.041$ geometry take the beam to 1 MeV/u for A=240. At this point a carbon stripper is used to increase the charge state to include a combination of 34+ to 36+ for A=240 in order to have increased beam current for further acceleration in 50 cavities of $\beta \sim 0.085$ geometry. Solenoid magnets are employed at the appropriate locations for beam focusing and to permit good operation with reasonable operating margins and low beam loss.

Component	f (MHz)	q/A Minimum	β In	β Out	Number	Voltage (MV) for A=240
Four Cavity Buncher	10 – 40	1/240	0.0008	0.0008	1	--
RFQ*	10	1/240	0.0021	0.0041	1	1.44
He Stripper* (Medium Ions)	--	--	0.0041	0.0041	1	--
IH DTL*	20.125	1/240	0.0041	0.0065	1	2.88
He Stripper (Heavy Ions)	--	1/66	0.0063	0.0063	1	--
Coax Cavity	40.25	1/66	0.0063	0.0063	1	0.077 Max
IH DTL	40.25	1/66	0.0063	0.015	1	4.8
$\beta=0.02$ SRF	80.5	1/66	0.015	0.024	16	11.4
$\beta=0.041$ SRF	80.5	1/66	0.024	0.047	34	42.6
C Stripper	--	1/8	0.047	0.047	1	--
$\beta=0.085$ SRF	80.5	1/8	0.047	0.129	50	49.4

Table 10. Parameters of the RIA post accelerator. (*Components on variable HV platform.)

4.3. Experimental Areas

The ISOL beams and those from the gas stopping station will serve two experimental areas. A ‘stopped beam’ area accommodates experiments that directly use the ISOL beams, for example ion and atom trapping experiments, laser spectroscopy, β -NMR, or decay studies (Figure 18). The size of the area is such that the experimental equipment proposed and discussed at the recent RIA detector workshop at Oak Ridge can be accommodated. The experimental area for the post-accelerated beams foresees a number of vaults for detectors and spectrometers (Figure 19). The number and size of the experimental vaults will be determined after the conclusions from ongoing discussions in the RIA user community have been drawn. In any case, the experimental areas can easily be expanded as needed.

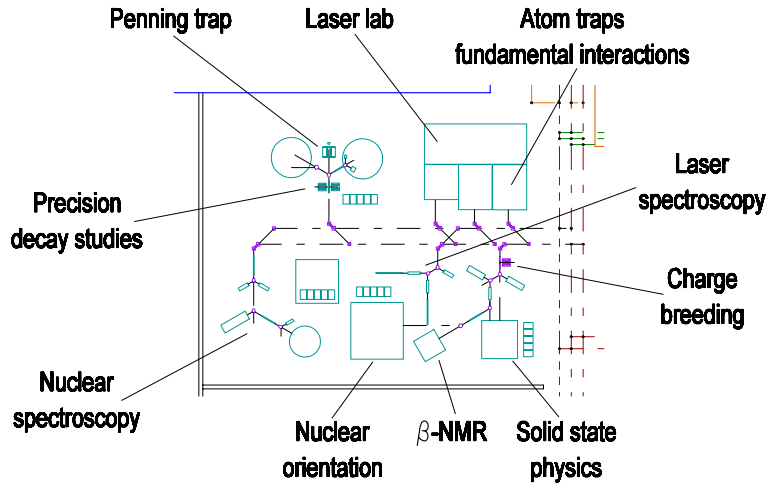


Figure 18: Schematic layout of stopped beam experimental area.

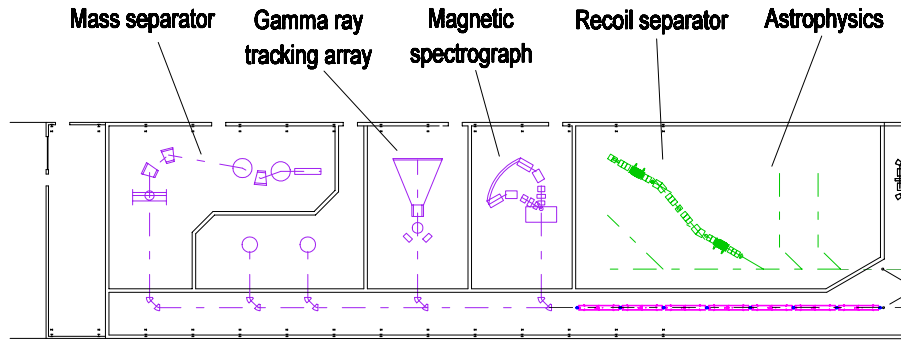


Figure 19: Schematic layout of the low-energy experimental area

5. In-flight Separation, Gas Stopping, and High-Energy Experiments

Two separators are envisioned for RIA [19]. One would deliver beams to a high-energy experimental area and could be very similar to the A1900 separator now operating at the NSCL. The second would deliver beams to an ion-catching station where the ions are slowed, thermalized, extracted, and sent to the post accelerator. The ion-catching station would use high-purity helium gas to stop the ions so that they remain charged and can be extracted quickly in a nearly chemically independent fashion. A momentum compensation section follows the second separator to reduce the range distribution of ions and allow most of the desired ions to be stopped in a reasonable gas volume [20]. The overall layout of the fragment separation area is shown in Figure 20. This layout has the advantage that the high acceptance separator can provide beams to either the gas stopping station or the high-energy area.

5.1. Production Targets

The targets needed for the production of fast beams at RIA have several significant constraints. To reduce the effect of geometric aberrations in the fragment separator that will limit collection efficiency in the gas-stopping cell and separation quality, the beam spot diameter should be <1 mm. Given that approximately 20% of the primary beam power is lost in the production target, the power densities in the target are extremely high, up to 500 kW/cm^3 (assuming a 400 kW primary beam). For projectile fragmentation, the ideal target has a low Z and hence has more atoms/cm² than a higher Z target, however, it is possible that for certain special cases, e.g. for Coulomb breakup, a higher Z target would be preferable. Prototype work is underway at ANL [21] for a windowless liquid lithium target suitable for heavy beams.

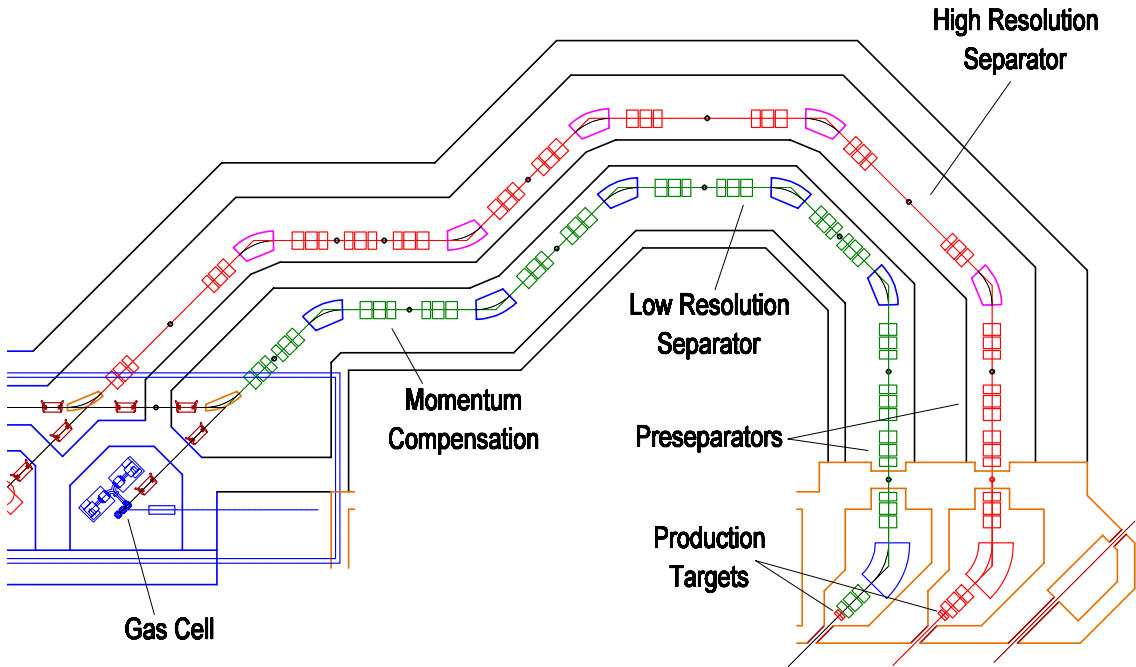


Figure 20. Baseline layout of the fragment separation area. Up to 400kW of primary beam strikes the production target. Two fragment separators can be used to deliver separated fragments to experimental areas. Each separator would consist of two stages of separation. A pre-separator would be used to collect the primary beam and unwanted fragments and the second stage separator would provide the final purification.

5.2. Fragment Separators

Baseline separator designs have been made for a high acceptance separator for the gas stopping station and a higher resolution separator to deliver beams to the fast beam area. The design goals are to achieve 10 T-m bending power with a 12% momentum acceptance and a 10 msr solid angle for the high efficiency separator and 6% momentum acceptance and 8 msr for the higher resolution separator. A full design of both separators that includes all limitations imposed by radiation hard magnets and the radiation fields of the beams dumps has not yet been made. The higher acceptance separator can

accommodate a large acceptance (and hence more contaminants) since the differing unwanted beams will stop at different depths in the ion catcher. A schematic layout of the fragment separators is shown in Figure 20.

Given the high radiation fields produced by 100 to 400 kW primary beams it is likely that the separators should have two stages: a pre-separator that removes most of the primary beam and other intense fragments, and the main separator that selects the ions of interest. Two stages of separation also significantly reduce impurity ions and most likely result in higher extraction efficiency for the gas-stopping cell.

A pre-separator will allow the removal of the primary beam and most unwanted fragments from the ions of interest. This reduces the radiation field outside the production area and also secondary interactions of ions that can cause significant background. Two stages of separation will significantly reduce the number of contaminant fragments that would pass into the gas cell [22]. The level of contaminants passing through the gas cell must not be too high and the reduction of unwanted ions will lead to higher extraction efficiencies. Ideally, the pre-separator would also allow the collection of unused isotopes for other applications. The separator optics will have a focus after the first dipole and the beam dump would be placed at this location. This area would also serve as a location for isotope recovery. A shielding wall separates the first part of the separator from the rest of the system. The whole system is achromatic and would operate as a standard fragment separator.

A full simulation of the radiation fields and power deposition has not yet been performed, but is essential. Significant R&D may be required to construct a 100 to 400 kW beam dump that can catch ions such as uranium. In addition, several percent of the primary beam may interact in the production target and produce kilowatts of other fragments that must be collected. The expected primary beam spot size at the location of the primary beam dump is 5 cm^2 in area and the stopping distance is as low as 1 cm. This results in a high power density and beam stop options need to be investigated. R&D on many aspects of the beam dump design is necessary.

The high-resolution separator would be very similar to the design of the A1900 at the NSCL. Considerable experience exists at the NSCL in the design and operation of this type of fragment separator and there are no significant challenges associated with meeting the desired 8 msr solid angle and 6% momentum acceptance. A higher momentum acceptance would increase the yield of a given fragment, but would also significantly increase the amount of contaminant ions. The current specification is set as a compromise between purity and rate.

5.3. Gas Stopping Station

The ideal catcher material is high-purity helium gas. The determination of what fraction of the incident projectile fragments can be extracted from a helium gas cell is close to being made. The NSCL gas cell is being tested and we have shown that we can implant on the order of 50% of the incident ions in 50 cm of 1-bar of helium. We have shown that the range-compression technique from GSI is workable with the appropriate beam

line. High-pressure gas (>1 bar) is very important for collecting projectile fragments, which only allows drifting the ions with static electric potentials. A prototype cell has been constructed at the NSCL and work is underway to optimize the extraction efficiency. The results so far seem consistent with calculations. An alternative gas cell is being designed by ANL to be tested at GSI. It relies on low-pressure helium (~ 150 mbar) and rf-potentials, but results are not yet available.

5.4. High Energy Experimental Area

Separated fast beams will be available following the high-resolution separator. Secondary beam energies of 50 to 400 MeV/nucleon (or more for lighter fragments) will allow a diverse experimental program. Based on input of the nuclear science community at workshops in LBL (1998) and ORNL (2003) it appears necessary to have a minimum of four high-energy experimental devices; a time-projection chamber for studies of compressed neutron matter, an implantation station for half live and decay studies, a gamma-ray detection station for Coulomb excitation and inelastic scattering studies, and a high-resolution momentum spectrometer with the capability to detect coincident neutrons at zero degrees. A possible layout of the high-energy experimental area is shown in Figure 21. The gas-stopping station was discussed previously.

The details of the design of the experimental devices will evolve with time, however the facility needs to incorporate space for the experimental equipment. The design shown in the figure also allows for future expansion.

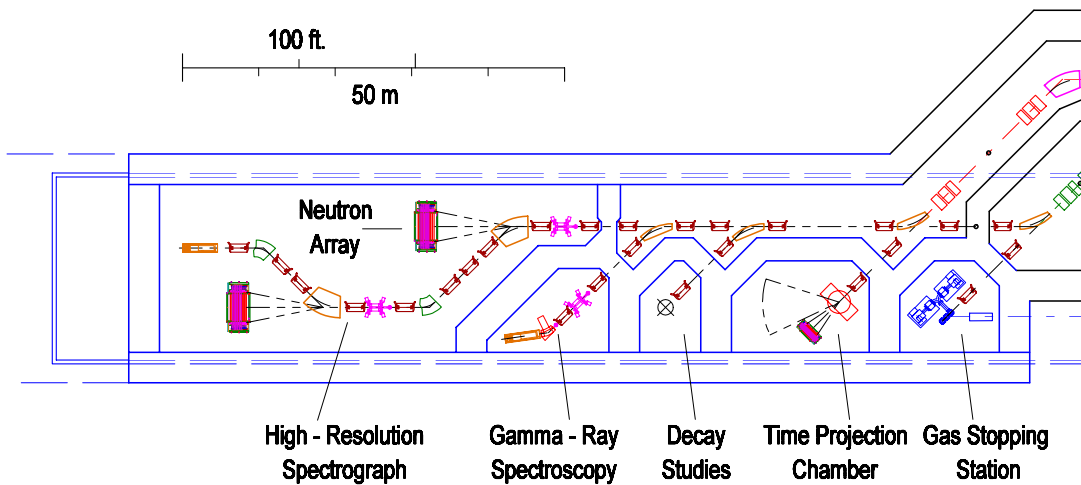


Figure 21. Schematic layout of the high-energy experimental area.

6. Summary

MSU has developed an overall conceptual design for the RIA facility with the goals of reducing technical and schedule risk while optimizing facility operational flexibility and reliability. Future emphasis will be placed on value engineering and implementation strategies to reduce initial facility costs while maintaining these goals.

7. References

1. R. Pardo, G. Zinkann, "Long-term Operating Experience for the ATLAS Superconducting Resonators", Proceedings of the IX Workshop on RF Superconductivity, Santa Fe, NM (1999), p 10-14.
2. A. Facco, V. Zviagnintsev, "Mechanical Stabilization of Superconducting Quarter Wave Resonators", Proceedings of the 1997 Particle Accelerator Conference, Vancouver (1997), p 3084-3086.
3. A.A. Kolomiets, V.N. Aseev, P.N. Ostroumov, P.C. Pardo, "Front End Design of the RIA Driver Linac", Proceedings of the 2003 Particle Accelerator Conference, Portland, OR 2003.
4. R. Duperrier, "Design of RFQ in favor of the RIA Project", NSCL internal report (2002).
5. D. Gorelov et al., "Analysis of a Multi-spoke Option for RIA Driver Linac", Proceedings of the 2003 Particle Accelerator Conference, Portland, OR 2003.
6. W. J. Scheider, P. Kneisel, C. H. Rode, "Gradient Optimization for SC CW Accelerators," Proceedings of the 2003 Particle Accelerator Conference, Portland, OR 2003.
7. R. A. Byrns & M. A. Green, "An Update on Estimating the Cost of Cryogenic Refrigeration," LBNL-40188, 1997.
8. P.N. Ostroumov, "Design Features of high-intensity medium-energy superconducting heavy-ion linac", Proceedings of the XXI Linac Conference, Gyeongju, Korea, 2002.
9. R. Duperrier, D. Gorelov, "Instabilities Study and Implication for the RIA Project", Proceedings of the 2003 Particle Accelerator Conference, Portland, OR, 2003.
10. X. Wu et al., "The Misalignment and RF Error Analyses for the RIA Driver Linac", Proceedings of the XXI Linac Conference, Gyeongju, Korea, 2002.
11. X. Wu et al. "The Beam Dynamic Studies of Combined Misalignments and RF Errors for RIA", Proceedings of the 2003 Particle Accelerator Conference, Portland, OR, 2003.
12. M. Portillo, et al., "Design Layout of an Isobar Separator based on 5th Order Calculations" Proceedings of the 2001 Particle Accelerator Conference, Chicago, IL, 2001.
13. R.E. Laxdal et al, "Beam Commissioning and First Operation of the ISAC DTL at TRIUMF", Proceedings of the 2001 Particle Accelerator Conference, Chicago, IL, 2001, p. 3942.
14. P.N. Ostroumov and A.A Kolomiets, "New Concept for Acceleration of Slow, Low Charge State Heavy Ion Beams", Proceedings of the 2001 Particle Accelerator Conference, Chicago, IL, 2001, p. 4077.
15. N.E Vinogradov et al, "Development of Room Temperature Accelerating Structures for the RIA", Proceedings of the 2003 Particle Accelerator Conference, Portland, OR, 2003.
16. K.W. Shepard, R.A. Kaye, B.E. Clifft, and M. Kedzie, "Beam Tests of the 12 MHz RFQ RIB Injector for ATLAS", Proceedings of the 1999 Particle Accelerator Conference, New York, NY, p. 525.
17. U. Ratzinger, "A Low Beta RF Linac Structure of the IH Type with Improved Radial Acceptance", LINAC 1988 Conference, Newport News, VA., p. 185.

-
18. W. Hartung et al, "Status Report on Multi-Cell Superconducting cavity Development for Medium-Velocity Beams", Proceedings of the 2003 Particle Accelerator Conference, Portland, OR, 2003.
 19. B.M. Sherrill, "Overview of the RIA Project", NIM B204 (2003) 765.
 20. H. Geissel et al., "Ions penetrating through ion-optical systems and matter", NIM A 282 (1989) 247.
 21. J. A. Nolen et al., "Development of windowless liquid lithium targets for fragmentation and fission of 400 kW uranium beams", NIM B204 (2003) 293.
 22. H. Geissel et al., "The super FRS project at GSI", NIM B204 (2003) 71.